APPLIED SCIENCES AND ENGINEERING

Persistent and responsive collective motion with adaptive time delay

Zhihan Chen[1] and Yuebing Zheng[1,2]*

It is beneficial for collective structures to simultaneously have high persistence to environmental noise and high responsivity to nontrivial external stimuli. However, without the ability to differentiate useful information from noise, there is always a tradeoff between persistence and responsivity within the collective structures. To address this, we propose adaptive time delay inspired by the adaptive behavior observed in the school of fish. This strategy is tested using particles powered by optothermal fields coupled with an optical feedback-control system. By applying the adaptive time delay with a proper threshold, we experimentally observe the responsivity of the collective structures enhanced by approximately 1.6 times without sacrificing persistence. Furthermore, we integrate adaptive time delay with long-distance transportation and obstacle-avoidance capabilities to prototype adaptive swarm microrobots. This research demonstrates the potential of adaptive time delay to address the persistence-responsivity tradeoff and lays the foundation for intelligent swarm micro/nanorobots operating in complex environments.

INTRODUCTION

Collective motion refers to the spontaneous emergence of coordinated behaviors among multiple interactive agents (*1*, *2*), observed in various natural systems such as bird flocks (*3*), fish schools (*4*), and locust swarms (*5*). Robotic systems also leverage collective motion to achieve complex tasks (*6*, *7*). Numerous factors influence the dynamics of collective motion, including density (*8*), perturbation (*9*), velocity (*10*), boundary (*11*), time delay (*12*–*20*), etc. Time delay is particularly important due to its intrinsic presence in every system, resulting from the finite information transmission speed among agents and the necessary information processing and execution time within each agent (*21*–*28*). Previous studies revealed that introduction of the fixed time delay led to interesting phenomena such as multistability, instabilities, and oscillations in collective motion (*29*–*32*), which provide an alternative explanation for observed collective behaviors in nature (*31*) and support advancements in swarm robotics (*33*). Notably, by incorporating proper time delay, the collective structures can have high persistence to maintain their movement in noisy environments (*30*, *34*). However, since most of the agents cannot efficiently distinguish nontrivial information (e.g., food sources and predators) from noise, the fixed time delay can also reduce the responsivity of collective structures, which slows down their global response to nontrivial external stimuli (*35*). Consequently, the fixed time delay in collective motion inherently leads to tradeoff between persistence and responsivity (*36*).

In this study, we propose adaptive time delay to effectively manage this persistence-responsivity tradeoff in collective motion. Adaptivity, which involves the ability to adapt to changes in external conditions, has been observed in diverse domains such as biology, physics, and social science (*37*). For the collective motion in nature, it has been found that fish groups can fine-tune their critical point in response to environmental risk and noise levels (*38*, *39*). Similarly, swarm robots can dynamically modulate their interaction strength in accordance with environmental cues for better stability and efficiency in their collective motion (*36*, *40*). Given the advantages of adaptivity in collective motion and that time delay is inherent in nearly all living and robotic systems, we hypothesize that the adaptive time delay, which merges adaptivity and time delay, could play a critical role in the adaptive behaviors observed in living species and offer a powerful approach to enhancing performance of swarm robots.

To validate the effectiveness of adaptive time delay in enhancing collective motion, we exploit both simulations and an optical feedback-control experimental platform to comparatively study the collective motion under the conditions of no time delay, fixed time delay, and adaptive time delay. Specifically, our experimental setup enables synchronous and flexible navigation of particles at an individual level, which can closely resemble the motion of living species through feedback control (*41*–*47*). This allows us to investigate how different time-delay conditions influence the collective motion in the real world. To better quantify the persistence of collective structures in experiments, we introduce a method called "active perturbation." Accordingly, by manipulating particle-particle interactions based on the time-delay Vicsek model (*12*, *30*, *31*, *35*), our experimental observations quantitatively confirm that a fixed time delay can enhance the persistence of collective structures against perturbations while diminishing their responsivity. However, when the time delay of each particle adapts to its surrounding environment, the collective structure can maintain its persistence while experiencing an approximate 1.6-fold increase in responsivity, implying a time saving of ~38% for the structure to reach the steady state. Furthermore, we demonstrate the advantage of adaptive time delay in improving the long-distance transportation and obstacle avoidance of collective structures in complex environments. These findings lay the groundwork for adaptive swarm micro/nanorobotics and showcase the potential of our platform in elucidating the role of adaptive time delay in the collective motion of living species.

RESULTS

Experimental setup and working principle

We begin by introducing our experimental platform, which enables feedback control of multiple particles based on programmable nonphysical interaction rules (Fig. 1A and fig. S1). Each particle's

[1]Materials Science and Engineering Program and Texas Materials Institute, The University of Texas at Austin, Austin, TX 78712, USA. [2]Walker Department of Mechanical Engineering, The University of Texas at Austin, Austin, TX 78712, USA.
*Corresponding author. Email: zheng@austin.utexas.edu

directional motion is driven by an individual laser beam (*48*), which can be instantaneously reoriented by adjusting the relative position between the beam center and the particle center (*49*). However, because of Brownian motion, the actual movement direction of the particle deviates from the ideal direction determined by the beam's position. In addition, variations in particle size result in different average speeds among the particles (fig. S2). Thus, our particle system can effectively mimic the behavior of living species or robots, which also move in noisy environments and exhibit heterogeneity among agents.

To enable time-delay interaction for each particle, real-time images are captured and stored in a sequential manner within the control program. This allows us to have a time-sequence history of each particle's positions, which is essential for implementing the nonphysical interaction between particles based on the time-delay Vicsek model (*12*, *30*, *31*, *35*). Specifically, the original Vicsek model posits that each particle determines its new direction by averaging the current velocities of itself and its neighbors, incorporating some random perturbation. This mechanism can give rise to ordered moving patterns, particularly at high particle density and low noise levels (*8*). In our adaptation, we maintain the velocity-alignment rule applied to all particles like the original Vicsek model. However, a departure from the original Vicsek model lies in the nonconstant magnitude of the velocity, and the noise term follows a Gaussian distribution owing to the nature of Brownian motion. Additional quantitative analysis supporting these modifications can be found in text S1. To introduce time delays into the Vicsek model, we assume that particles can calculate their new directions based on the past velocities of themselves and their neighbors. Time delays can be classified into two categories: transmission time delay, resulting from the finite speed of information transmission among agents, and response time delay, arising from the finite speed of information processing and execution within each agent (*31*). Mathematical descriptions of these time delays and their integration into the model can be found in Materials and Methods. In addition, we incorporate volume exclusion and reflective boundary into our feedback control program (Materials and Methods) to prevent particle collisions and maintain cohesion of collective structures, respectively. For enhanced clarity, the definitions of existing variables and the parametric conditions for each experimental or simulated implementation in the study are available in tables S1 and S2.

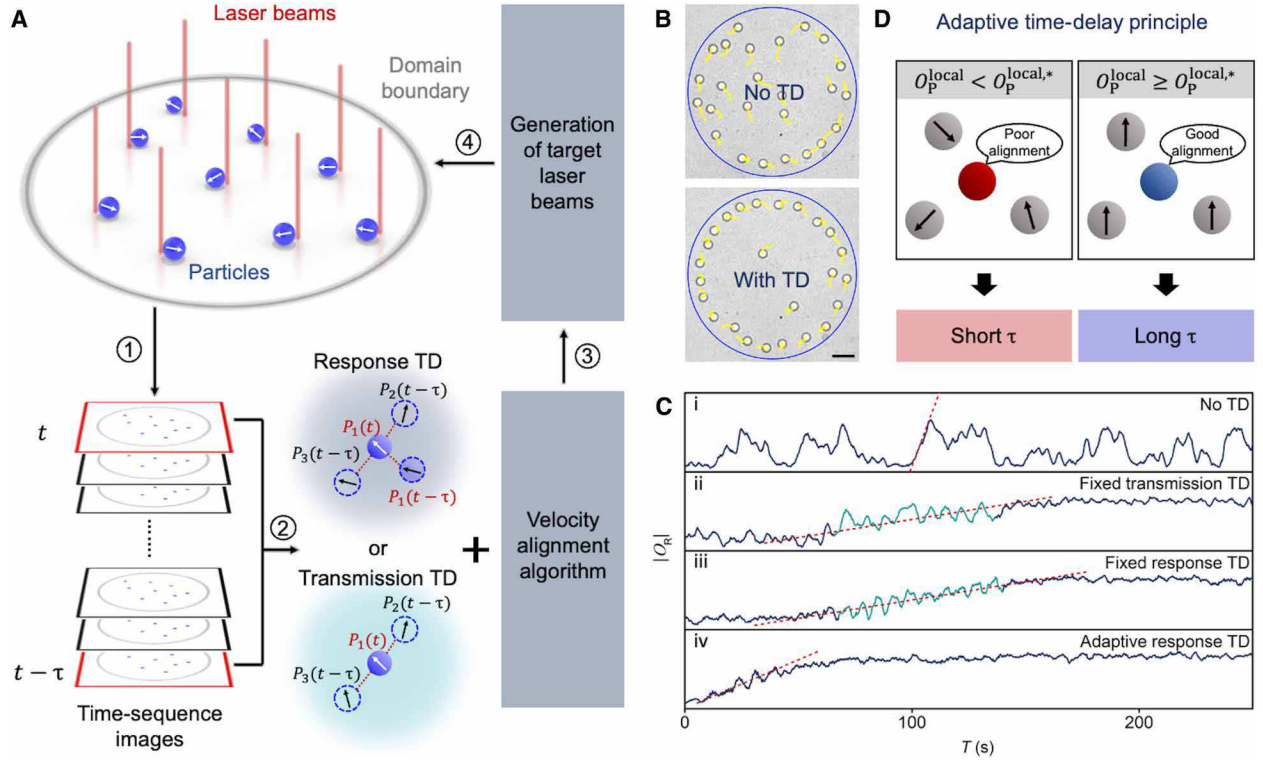

Fig. 1. Collective motion of light-powered particles with adaptive time delay investigated by an optical feedback-control platform. (**A**) Schematic of the feedback control setup. Independent laser beams power the particles, and their real-time images are captured and stored. The program calculates the next moving directions of each particle based on the time-delay Vicsek model, and the updated hologram is transferred to the spatial light modulator (SLM) to control the target laser beams. The numbers "1" to "4" on the arrows represent the steps of optical imaging capture, imaging analysis, SLM control, and optical manipulation, respectively. In the schematic depicting two types of time delay, the solid circles represent the target particles, while the dashed circles represent the neighboring particles. The symbol "*P*" indicates the moving states of the particles. The mathematical definitions of response and transmission time delays can be found in Eqs. 3 and 4. (**B**) Optical images of the collective motion without time delay (top) or with fixed (transmission/response) time delay (bottom). Scale bar, 5 μm. (**C**) $|O_R|$ versus time for different time-delay conditions. The blue curves are smoothed using an average with a span of 20 timesteps. The green segments highlight the oscillation phenomena, while the red dashed lines represent the speed at which the system reaches the steady states. (**D**) Schematic of the working principle of adaptive time delay. The arrows show the moving directions of the agents. The fixed transmission/response time delay used in (B), [C(b)], and [C(c)] is denoted as 1.0τ*. The adaptive response time delay in [C(d)] involves long $\tau = 1.0\tau^*$, short $\tau = 0.1\tau^*$, and $O_P^{local,*} = 0.6$. TD, time delay.

To assess the impact of time delay on collective motion within perturbed real environments, we performed experiments involving 25 particles within a circular domain with a radius (r_b) of 20.0 μm. The chosen time delay value (τ) is set at $\tau = \tau^* \cong \frac{r_0}{|\mathbf{v}_{avg}|}$ (*30*), where r_0 represents the radius of velocity alignment, which is set as 7.75 μm if without further clarification. The term $|v_{avg}|$ denotes the average particle velocity under specific laser power and laser-particle distance conditions, whose value is set as 1.16 μm/s here (text S1). In experiments, each loop is subject to an execution time derived from various instruments, designated as $\Delta t = 0.132\ s$. Consequently, we establish τ in our experiments by setting $\tau = n_\tau * \Delta t$, where n_τ is adjustable as any positive integer. The spatiotemporal patterns observed in experiments, i.e., rotating collective structures around the center of the confined circular geometry, indicate that both transmission and response time delays promote more persistent and ordered collective motion compared to motion without time delay (Fig. 1B and movie S1). To quantitatively assess the impact of time delay on collective motion, we use the rotation order parameter, $O_R = \frac{1}{N}\sum_{i=1}^{N} \hat{\mathbf{v}}_i \times \hat{\mathbf{r}}_{i-b}$ (*50*), where N denotes the total number of particles, and $\hat{\mathbf{r}}_{i-b}$ represents the unit vector from the center of the particle to the center of the confined geometry. The absolute value of O_R ranges from 0 to 1, indicating the group's degree of rotation. By performing parametric sweeping of the fixed τ, our experimental observations reproduce two distinctive features of time-delay collective motion, which are consistent with the predictions by several previous simulation studies (*12*, *30*, *35*). First, the time-averaged $|O_R|$ ($\langle|O_R|\rangle$) initially increases and then decreases as τ increases (figs. S3 and S4A). This behavior is attributed to the fact that time delay initially helps collective structures resist noise at small τ values but hinders particle alignment at large τ values (*12*). Second, the observed oscillations in $|O_R|$ arise from the echoing of information due to delayed interactions, a characteristic feature of delay dynamical systems (*12*, *51*). Their periodicity (figs. S3 and S4B) can be accurately described by the linear function periodicity = $\tau + \Delta t$ (*12*, *35*).

Upon further examining $|O_R|$ over time under different time-delay conditions, we observe some distinct behaviors. Without time delay, $|O_R|$ exhibits strong fluctuations due to Brownian motion (Fig. 1C, a), which indicates that the collective structure is noisy and at the dynamic phase transition (fig. S5). In contrast, collective motion with a fixed time delay demonstrates a persistent rotation around the center of the confined geometry once it reaches a steady state (Fig. 1C, b and c). An induction period observed previously (*30*) is also found here, arising from the slow velocity alignment induced by the long fixed time delay. To confirm that the observed persistent motion is indeed due to the introduction of time delay, we dynamically vary τ within the same experimental realization and observe the corresponding changes in $|O_R|$ (movie S2). The switch between fluctuation and a stable rotation of the same collective structure under different τ values validate that persistent collective motion directly results from the introduction of time delay (fig. S6). In addition, as the responsivity of a collective structure reflects the rate at which it responds to the perturbation and approaches the presumed steady state (*35*, *36*), we adopt the straightforward definition of $d|O_R|/dt$ to quantify the collective structures' global response speed, i.e., their responsivity, in this study. An R-fold increase in responsivity implies that the collective structure can reach the steady state $\frac{R-1}{R} * 100\,\%$ faster. Because of the tradeoff between persistence and responsivity, $d|O_R|/dt$ decreases substantially as τ increases (red dashed lines in Fig. 1C).

In natural systems, fish schools have been observed to adjust their distance to criticality to manage the persistence-responsivity tradeoff (*38*, *39*). One hypothesis suggests that fish starts to startle when the accumulated stochastic activation cues from their neighbors exceed a certain threshold (*39*). This implies that fish can adjust their "sensitivity" to their local environment, ensuring that the school of fish adapts its movements only in response to sufficiently strong cues. Inspired by this concept, we introduce the concept of sensitivity to time delays, which is common in both living and artificial systems, to propose an adaptive time-delay strategy that enhances the responsivity of collective structures while maintaining high persistence. The time delay of collective structures can be made adaptive through different mathematical definitions. In accordance with Ockham's Razor, we propose a straightforward approach where a threshold of the local polarization order parameter ($O_P^{local,*}$) is used to determine the transition between short τ and long τ for individual particles (Fig. 1D). The value of τ at time t is determined by

$$\tau(t) = \begin{cases} \text{short}\,\tau, O_P^{local}(t-\Delta t) < O_P^{local,*} \\ \text{long}\,\tau,\ O_P^{local}(t-\Delta t) \geq O_P^{local,*} \end{cases} \quad (1)$$

$$O_P^{local} = \frac{1}{N_{local}} |\hat{v}_i + \sum_{j \in C_i} \hat{\mathbf{v}}_j| \quad (2)$$

C_i represents the circular neighborhood around particle i, excluding particle i itself. For simplicity, we let it have the same radius as the velocity-alignment zone (i.e., r_0). N_{local} is the total number of neighboring particles plus particle i itself. Here, O_R is not used because agents, such as living species or robots, may not have access to global information like the center of the confined geometry. However, they can continuously assess the translational motion of their neighbors. When the O_P^{local} of an agent exceeds a predefined threshold $O_P^{local,*}$, it indicates well-aligned velocities of the surrounding agents, representing an ordered local environment. In this case, the agent adopts a large τ. Conversely, when $O_P^{local} < O_P^{local,*}$, the agent experiences a relatively disordered local environment, leading to a short τ. It should be noted that the adaptive time delay is based on the response time delay, as the transmission time delay typically depends on environmental conditions, such as the speed of light, sound, or chemical diffusion, which cannot be actively tuned by the agents. Therefore, our discussion about adaptive time delay focuses on modulating the response time delay, which is likely to be controlled internally by living species or robots. Besides, the value of short τ, long τ, and $O_P^{local,*}$ in Eqs. 1 and 2 can be specific to every system and might be varied for different collective structures. By implementing the adaptive time delay in our experimental platform with an appropriate $O_P^{local,*}$, the collective structure can resist the influence of particle motion fluctuations as those with a fixed time delay while also having higher $d|O_R|/dt$ (Fig. 1C, b and d). This initial finding suggests that the introduction of adaptive time delay has the potential to generate collective motions that are both persistent and responsive.

Active perturbation for persistence characterization

To quantitatively analyze how adaptive time delay manages the persistence-responsivity tradeoff in collective motion, we first introduce an active perturbation method to assess the persistence of collective motion, similar to $d|O_R|/dt$ for the responsivity. Persistence

measures the collective structure's ability to maintain its original motion in the face of stimuli. Ideally, the collective structures should be able to withstand trivial perturbations, such as environmental noise (line "1" in Fig. 2A) while also adapting their motion in a controlled manner without collapsing when encountering nontrivial perturbations, such as predators or food sources (lines "2" and "3" in Fig. 2A). Moreover, the response represented by line 2 is superior to that of line 3 as it demonstrates faster adaptation to nontrivial stimuli. For microparticles in a fluidic environment, it is essential to attenuate their inherent Brownian motion for persistent collective motion. Experimental measurements demonstrate that the influence of Brownian motion decreases rapidly as the observation time increases due to its stochastic nature (Fig. 2B and text S1). Therefore, if we consider Brownian motion as a type of perturbation with the observation time being Δt_{ob} ($\Delta t_{ob} = n_{ob} * \Delta t$ with n_{ob} being any positive integer), then its influence can be minimized by increasing Δt_{ob} (Fig. 2B). Meanwhile, as shown in Fig. 1 and fig. S4, a properly long τ in the collective structure can effectively eliminate the influence of Brownian motion, leading to much more persistent collective motion. On the basis of this observation, we assume that, when τ is comparable with or larger than the perturbation's duration time, the impact of this perturbation can be eliminated.

For the active perturbation method, it allows us to activate various types of perturbations with arbitrary duration times (ΔT_P) during the ongoing collective motion. Different active perturbations can be achieved in our platform by emulating scenarios that occur in living or robotic systems, such as certain particle(s) having abnormally higher velocity, suddenly losing navigation ability or moving in specific directions like the living species finding food or predators (text S3 and movie S3). To better quantify the persistence of collective structures while avoiding any particle collision, we design an active perturbation where a particle is directed toward the center of the confined geometry within certain ΔT_P (Fig. 2C). This perturbation aims to reduce the value of $|O_R|$, as indicated by the expression of O_R. As particles are programmed to align their velocities with their neighbors, the maximum reduction in $|O_R|$ ($\Delta|O_R|_{max}$) can serve as a metric to quantify the total impact of this active perturbation and characterize the persistence of the collective structures (Fig. 2D) (*36*). Specifically, $\Delta|O_R|_{max}$ represents the difference between $|O_R|$ at the onset of the active perturbation and the minimum $|O_R|$ observed during the effective time period of the perturbation. A higher $\Delta|O_R|_{max}$ indicates a lower level of persistence in the collective structure.

In the experiments, we exploit the active perturbation method with different ΔT_P values in collective structures that have τ values

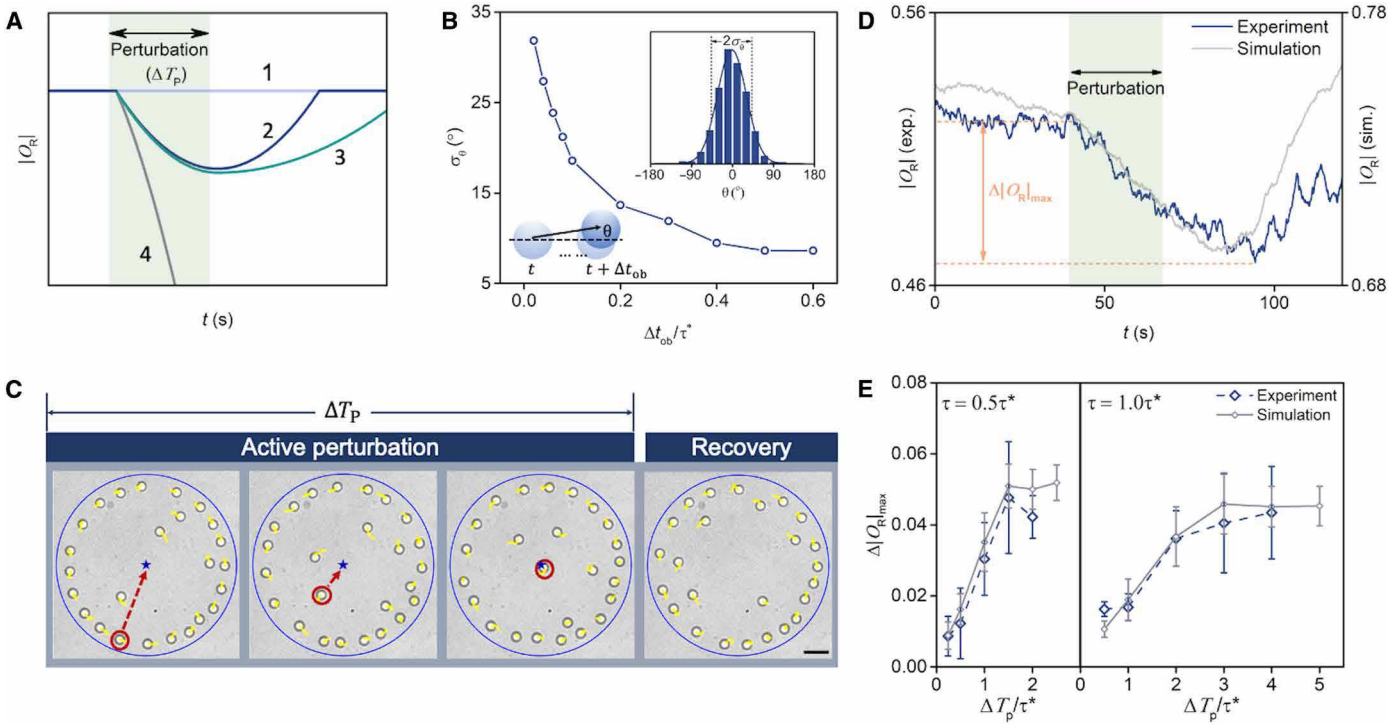

Fig. 2. Investigation on the time-delay–enhanced persistence using the active perturbation method. (**A**) Schematic demonstrating four possible conditions when collective motion encounters a perturbation with duration time ΔT_P. (**B**) The SD of the angle deviation (σ_θ) of a single particle's motion perturbed by Brownian motion versus the observation time (Δt_{ob}) normalized by τ^*. Δt_{ob} can be equal to the perturbation duration time ΔT_P. The bottom-left inset shows that the Brownian motion will deviate the particle's moving direction by an angle θ within certain Δt_{ob}. The top-right inset indicates that θ can be fitted by the normal distribution. (**C**) Time-sequence optical images showing the execution of an active perturbation, where one particle is forced to move toward the center of the circular confined geometry. After ΔT_P, the perturbed particle recovers its interaction with the neighboring particles. Scale bar, 5 μm. (**D**) The change of $|O_R|$ with a fixed response time delay $\tau = 1.0\tau^*$ when an active perturbation with $\Delta T_P = 4.0\tau^*$ is implemented. The curves are smoothed by using an average with a span of 200 timesteps. (**E**) $\Delta|O_R|_{max}$ versus $\Delta T_P/\tau^*$ for collective structures with fixed response time delay $\tau = 0.5\tau^*$ (left) and $\tau = 1.0\tau^*$ (right). The active perturbation types in (D) and (E) are the same as that shown in (C). All the error bars indicate the SD.

of 0.5τ* and 1.0τ*, respectively (Fig. 2E). The simulations were also carried out using agent-based modeling. The parameters governing the agents' movement, such as Brownian motion, velocity, particle heterogeneity, and long-range physical interactions (texts S1 and S2), were quantified through experimental data and subsequently incorporated into the simulations. Thus, our simulations encompass velocity alignment, noise, heterogeneity, and optothermal-induced long-range physical interactions (Materials and Methods) while excluding considerations of hydrodynamic coupling and complex concentration profiles of solutes (text S4). Both the simulations and experiments consistently show that as the τ value increases, the observed $\Delta|O_R|_{max}$ decreases under the same ΔT_P, suggesting a positive correlation between τ and the persistence of collective structures (fig. S7A). This correlation can be attributed to the fact that the time delay hinders information propagation among particles (*12*, *35*), reducing the influence of any perturbation on the collective structure. As a result, the global change (e.g., $\Delta|O_R|_{max}$ in our current system) in the collective structure becomes smaller. In addition, we observe a saturation of $\Delta|O_R|_{max}$ as ΔT_P increases. This saturation occurs because when ΔT_P is sufficiently long, the perturbed particle reaches the vicinity of the center of the confined geometry. In this region, the perturbed particle becomes less correlated with the rest of the particles (Fig. 2C), limiting its influence on the collective motion. Accordingly, we can explain our assumption that the effect of Brownian motion on collective motion can be reduced by the time delay. If Brownian motion is treated as a perturbation with a short ΔT_P, then its capacity to induce disorder in the collective structures is high (Fig. 2B). However, the impact of this perturbation with a short ΔT_P is minimized when the collective structure has an appropriately long-time delay (Fig. 2E and fig. S7B). In contrast, if Brownian motion is considered as a perturbation with a long ΔT_P, although its influence will not be easily mitigated by the time delay this time, then its impact is substantially reduced at longer ΔT_P (Fig. 2B), which still cannot influence the collective motion much. Thus, the application of a suitable time delay to the collective structure leads to a reduction in the influence of Brownian motion (*30*, *35*).

In summary, by having an appropriate time delay, collective structures can exhibit high persistence, preventing the system from being overly sensitive to environmental noise. However, since the particles cannot differentiate the nontrivial information from noise, this increase in persistence comes at the cost of reduced responsivity, as the time delay not only filters out noise but also hinders the alignment among particles.

Characterization and management of persistence-responsivity tradeoff

The intrinsic tradeoff between persistence and responsivity in collective motion can be managed through the bio-inspired adaptive time-delay strategy (Fig. 1D). By measuring $\Delta|O_R|_{max}$ and $d|O_R|/dt$ under different fixed response time delays, we first confirm the existence of the persistence-responsivity tradeoff (Fig. 3A, a and b). It is important to note that $\Delta|O_R|_{max}$ cannot be accurately measured if the fixed time delay is too short or too long. When τ is too short, the influence of particle motion fluctuation is not substantially reduced, and it overlaps with the effect of active perturbation, thereby disturbing the measurement of $\Delta|O_R|_{max}$ (fig. S7B). Conversely, when τ is too long, it removes the influence of both particle motion fluctuation and active perturbation with certain ΔT_P, resulting in no change observed in $\Delta|O_R|_{max}$ (fig. S7B).

To assess the effectiveness of the adaptive time-delay strategy in our current system, we conduct a parametric study to identify a suitable $O_P^{local,*}$, at which the persistence is ensured to remain intact while a considerable enhancement in responsivity can be achieved. Here, the long and short τ are fixed at 1.0τ* and 0.1τ*, respectively. The long τ is chosen according to fig. S4A, at which the motion fluctuation of individual particles is attenuated but the velocity alignment is not substantially hindered. The short τ is not set to zero here in consideration that the response time delay cannot be eliminated in living species and robots. The experimental results in Fig. 3A(c) show that $\Delta|O_R|_{max}$ remains constant until $O_P^{local,*}$ reaches a value of approximately 0.4, after which it shows the rising trend. This observation can be explained by considering the number of particles in the collective structures that have short τ (Fig. 3B). Even at the steady state, because of motion fluctuations and the curvature of the circular boundary, O_P^{local} of each particle cannot reach 1. Therefore, when $O_P^{local,*}$ is set too high, many particles constantly have short τ at the steady state even if there is no nontrivial information (Fig. 3C). These particles facilitate the transmission of various types of information, including motion fluctuations, thereby reducing the persistence of the collective structures. In contrast, regarding the relationship between responsivity and $O_P^{local,*}$, Fig. 3A(d) demonstrates that $d|O_R|/dt$ monotonically increases as $O_P^{local,*}$ increases from 0 to 1. This is because higher values of $O_P^{local,*}$ result in a greater number of particles with short τ in both transient and steady states (Fig. 3B). Consequently, information can spread more rapidly within the collective structures, leading to faster global shifts in response to external changes. Accordingly, the suitable $O_P^{local,*}$ in experiments is 0.4, where the persistence is ensured to be maintained while the responsivity is enhanced by approximately 1.6 times (i.e., saving ~38% time to reach the steady state).

The simulations closely align with the experiments, which show approximately 1.4-times improvement in responsivity (i.e., saving ~29% time to reach the steady state) without sacrificing persistence. Moreover, simulations also display the trend that the persistence starts to decrease when the set $O_P^{local,*}$ exceeds a critical value where the average number of particles with short τ starts growing fast (Fig. 3C). However, there exists a numeric variance in the suitable value of $O_P^{local,*}$, represented by two different stars in Fig. 3 [A(c) and C]. In Fig. 3C, "simulation condition 2" introduces the laser-positioning error, while "simulation condition 3," based on simulation condition 2, adds the detection error (text S4). These three simulated curves illustrate that, as the simulations incorporate a broader array of factors present in actual experiments, the simulated results more closely approximate the experimental measurements. Despite a thorough consideration of numerous factors, there remain several inherently challenging elements that cannot be integrated into the simulations, as detailed in text S4. Consequently, this inherent complexity leads to a persistent numeric mismatch in Fig. 3C. In addition, the numeric deviation observed in Fig. 3A(d) can be directly traced back to the distinctions highlighted in Fig. 3C, as illustrated in fig. S8.

Combining experimental and simulated results, we reveal a general protocol to find a suitable $O_P^{local,*}$ for certain collective structures, which will measure the average number of particles with short τ under different $O_P^{local,*}$ and then identify the value where this average approaches 1 as closely as possible. Specifically, the adaptive

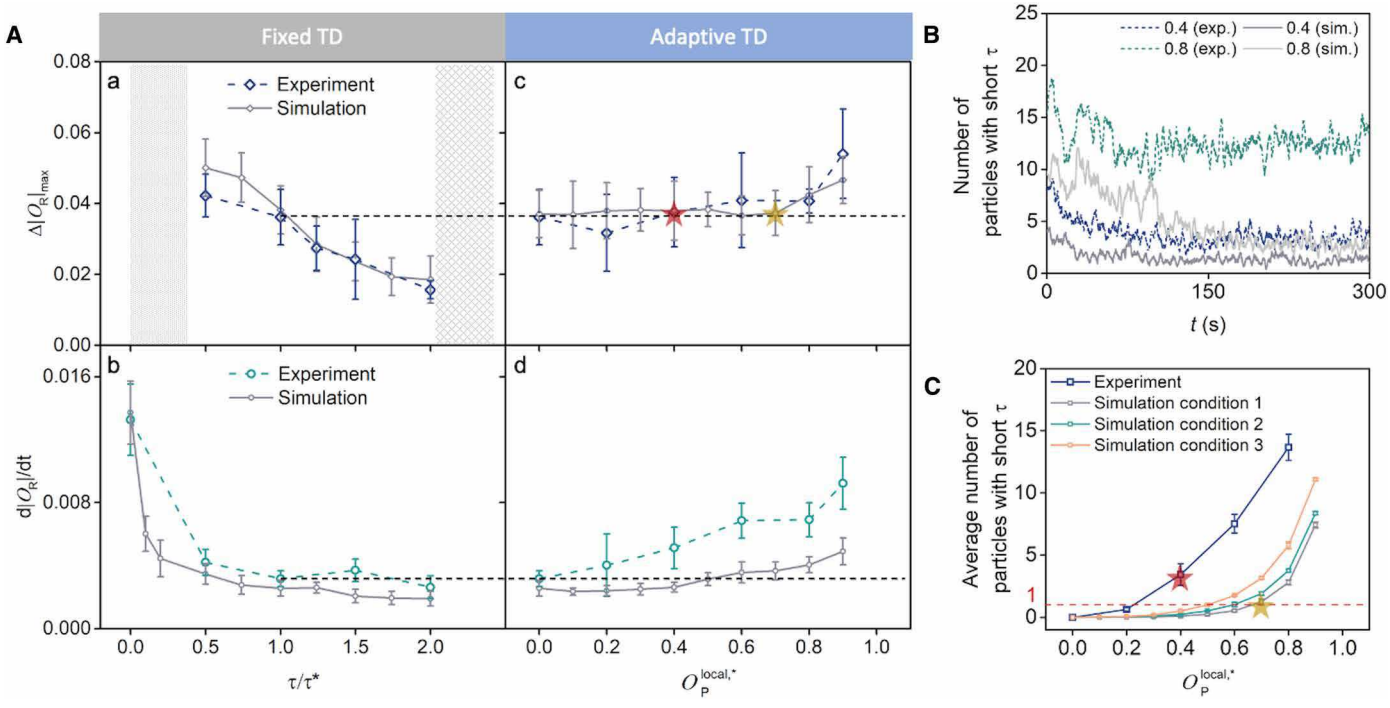

Fig. 3. Enhancing responsivity of collective structures without sacrificing persistence by the adaptive time-delay strategy. (**A**) Experimental and simulated results showing the persistence-responsivity tradeoff under the fixed responsive time delay (a and b) and the improvement made by the adaptive time-delay strategy (c and d). ΔT_P is set to be 2.0τ* for all the measurements in (a) and (c). The two shadow regions in (a) imply that $\Delta|O_R|_{max}$ cannot be measured either because the time delay is too short (left region), which fails to eliminate the influence of particle motion fluctuation, or too large (right region), where the effect of active perturbations with a fixed ΔT_P = 2.0τ* cannot be observed. The suitable $O_P^{local,*}$ values are determined for both the experiments (red star) and simulations (yellow star). (**B**) Number of particles with short τ as a function of execution time. The two dashed lines represent experimental realizations with $O_P^{local,*} = 0.4$ (blue) and $O_P^{local,*} = 0.8$ (green), respectively. The corresponding simulated results are shown as two gray solid lines. The curves are smoothed using an average with a span of 20 timesteps. (**C**) Average number of particles with short τ plotted against $O_P^{local,*}$. The values are obtained by averaging the number of particles with short τ at the steady state of collective motion, i.e., the data after 200 s in (B). The red and yellow stars in (C) indicate the same $O_P^{local,*}$ as those shown in [A(c)]. Simulation condition 1 includes the particle's motion fluctuation and heterogeneity. Condition 2 incorporates additional laser-positioning deviation into the simulations, while condition 3 further increases the particle's motion fluctuation by 1.5 times compared to the condition 2. The simulations in (A) are based on the simulation condition 1. The error bars indicate the SD.

time-delay strategy uses long τ to eliminate noise and short τ for a fast response to nontrivial information. Excessive $O_P^{local,*}$ can result in some particles constantly having short τ, even in noisy environments without any nontrivial events, facilitating noise transmission and lowering persistence. Conversely, if $O_P^{local,*}$ is too low, then particles become too inert to respond to nontrivial information. Therefore, for different collective structures, we aim to find $O_P^{local,*}$ where the average number of particles with short τ approaches 1 as closely as possible. Notably, experimental results suggest that $O_P^{local,*}$ exceeding the value determined by this protocol can sometimes result in better performance (Fig. 3C). Nevertheless, this protocol remains effective, which consistently ensures that persistence is never compromised while responsivity, although not optimized, can still be improved. For example, if we strictly follow this protocol, then $O_P^{local,*}$ should be 0.2 for experimental results, where the responsivity can still be enhanced by about 1.3 times. Furthermore, although directly characterizing persistence and responsivity provides a more precise determination of $O_P^{local,*}$, the definitions of these parameters can vary among different collective structures (*36*). In contrast, measuring the average number of particles with short τ is more accessible and general, requiring only the agents' temporal velocities to determine their time-delay status based on Eqs. 1 and 2. In practice, we can initially determine $O_P^{local,*}$ using the proposed "one-agent-with-short-τ" rule. If necessary, we can then define and quantify persistence and responsivity to further refine $O_P^{local,*}$ for different collective structures.

To validate the effectiveness and universality of the adaptive time-delay strategy and the corresponding protocol to determine $O_P^{local,*}$, we conducted diverse simulations and experiments under varying interaction radii, boundary sizes, particle numbers, and different moving patterns. First, the adaptive time-delay strategy proves effective when the interaction radius (r_0) and boundary size (r_b) vary (Fig. 4, A to C). Responsivity increases as $O_P^{local,*}$ grows (Fig. 4B), and the group's persistence remains stable until $O_P^{local,*}$ exceeds the critical value (Fig. 4A) where the average number of particles with short τ is around 1 (Fig. 4C). Simulations with different particle densities exhibit the similar trend (fig. S9). Notably, the strategy is ineffective at low particle densities (e.g., $N < 15$ with $r_b = 20.0$ μm), as sparse velocity alignment among particles fundamentally impedes the formation of ordered collective structures. Experiments under different particle numbers (movie S4) and a complex boundary shape (movie S5) further validate the effectiveness of the adaptive time-delay strategy (fig. S10).

Furthermore, our simulation results underscore the effectiveness of the adaptive time-delay strategy within the context of two-dimensional

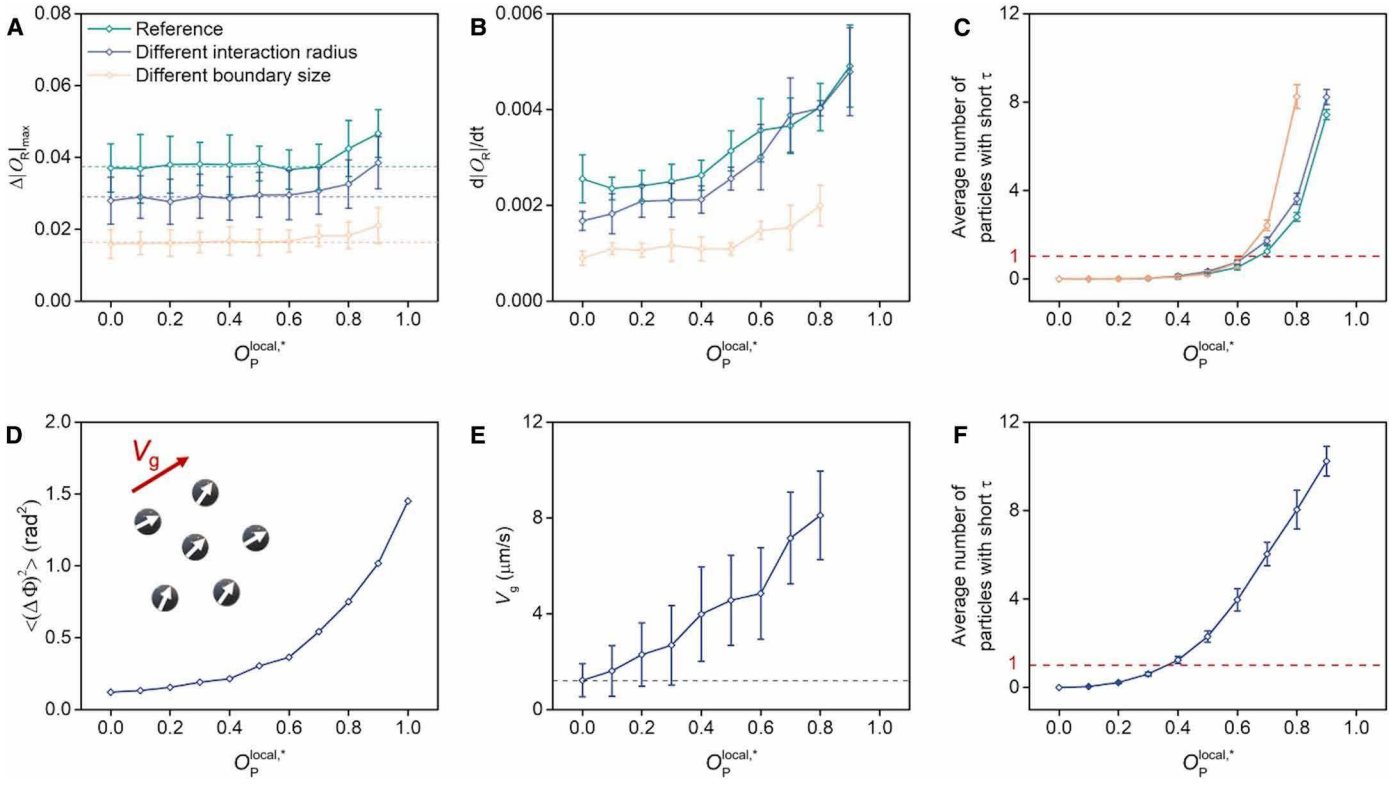

Fig. 4. Efficacy of the adaptive time-delay strategy in variable conditions. (**A**) The simulated persistence ($\Delta|O_R|_{max}$), (**B**) responsivity ($d|O_R|/dt$), and (**C**) average number of particles with short τ versus different $O_P^{local,*}$ when the adaptive time-delay strategy is implemented under different interaction radii (r_0) and boundary sizes (r_b). The "Reference" and "Different interaction radius" conditions feature only one perturbed particle during active perturbation, while the "Different boundary size" condition includes two perturbed particles to achieve a larger $O_P^{local,*}$ and minimize numeric errors. (**D**) The simulated indicator of persistence [$\langle(\Delta\phi)^2\rangle$], (**E**) group velocity V_g, and (**F**) average number of particles with short τ versus different $O_P^{local,*}$ when the adaptive time-delay strategy is implemented under the translational collective motion in open space. $\Delta\phi$ represents the angle deviation between the initial and subsequent directions of the collective structure after certain intervals (fig. S11B). The numeric parameters in this figure are listed in table S2, while the simulation details for translational collective motions are provided in Materials and Methods.

translational collective motion in open space, as demonstrated in Fig. 4 (D to F) and movie S6. The traditional Vicsek model without any time-delay mechanism rapidly forms ordered configurations yet struggles with maintaining consistent directionality owing to perturbations from Brownian motion (fig. S11). Alternatively, implementing a fixed time delay counters the effects of Brownian motion but at the expense of diminished group velocity due to reduced responsivity. The integration of an adaptive time delay presents a substantial improvement, enabling the collective structure to preserve its moving direction while achieving a group velocity that is triple that of the fixed time-delay scenario (movie S6 and Fig. 4, D and E). Notably, the enhanced $O_P^{local,*}$ persists at the value where the average number of particles with short τ is around 1 (Fig. 4F), supporting our proposed one-agent-with-short-τ rule.

To conclude, the adaptive time-delay strategy and the method to determine suitable $O_P^{local,*}$ exhibit broad applicability. However, it is essential to note that the absolute value of $O_P^{local,*}$ may vary substantially due to diverse parameters of collective structures such as density, interaction radius, boundary size, etc. Thus, this value needs to be specifically determined for different collective structures.

Demonstration of adaptive optical swarm microrobots

Last, the adaptive time-delay strategy enables the persistent and responsive transportation of collective structures in complex environments (Fig. 5A). The manipulation of the motorized stage is added to the automated feedback control program, enabling the precise delivery of collective structures in two dimensions over long distances. In addition, an algorithm is developed to effectively guide the particles to bypass encountered obstacles (text S5). To demonstrate the transportation capability, a collective structure is sequentially guided through three sets of obstacles with different sizes and distributions (Fig. 5B and movie S7). Notably, these obstacles are defined by the program, allowing for arbitrary adjustment of their properties and facilitating rapid prototyping of collective motion in diverse complex environments. On the basis of this, we conduct experiments where the collective structures are directed to pass through three obstacles arranged in a triangular configuration under different time-delay conditions (Fig. 5C and movie S8). Here, we set $O_P^{local,*} = 0.4$ for the adaptive time-delay condition, as determined in Fig. 3. Moreover, this value can consistently be used for arbitrary obstacle configurations as the choice of $O_P^{local,*}$ is proved to be independent of the sizes or morphologies of the obstacles (text S5). The $|O_R|$ versus time curves are plotted (Fig. 5D) and show that the collective structure with adaptive time delay displays quick responses to the obstacles while maintaining persistent motion when not interacting with the obstacles. Moreover, after passing the obstacles, the collective structure with the adaptive time delay reaches the steady state faster compared to those with fixed time delays or no time delay. Therefore, the adaptive time-delay strategy allows for

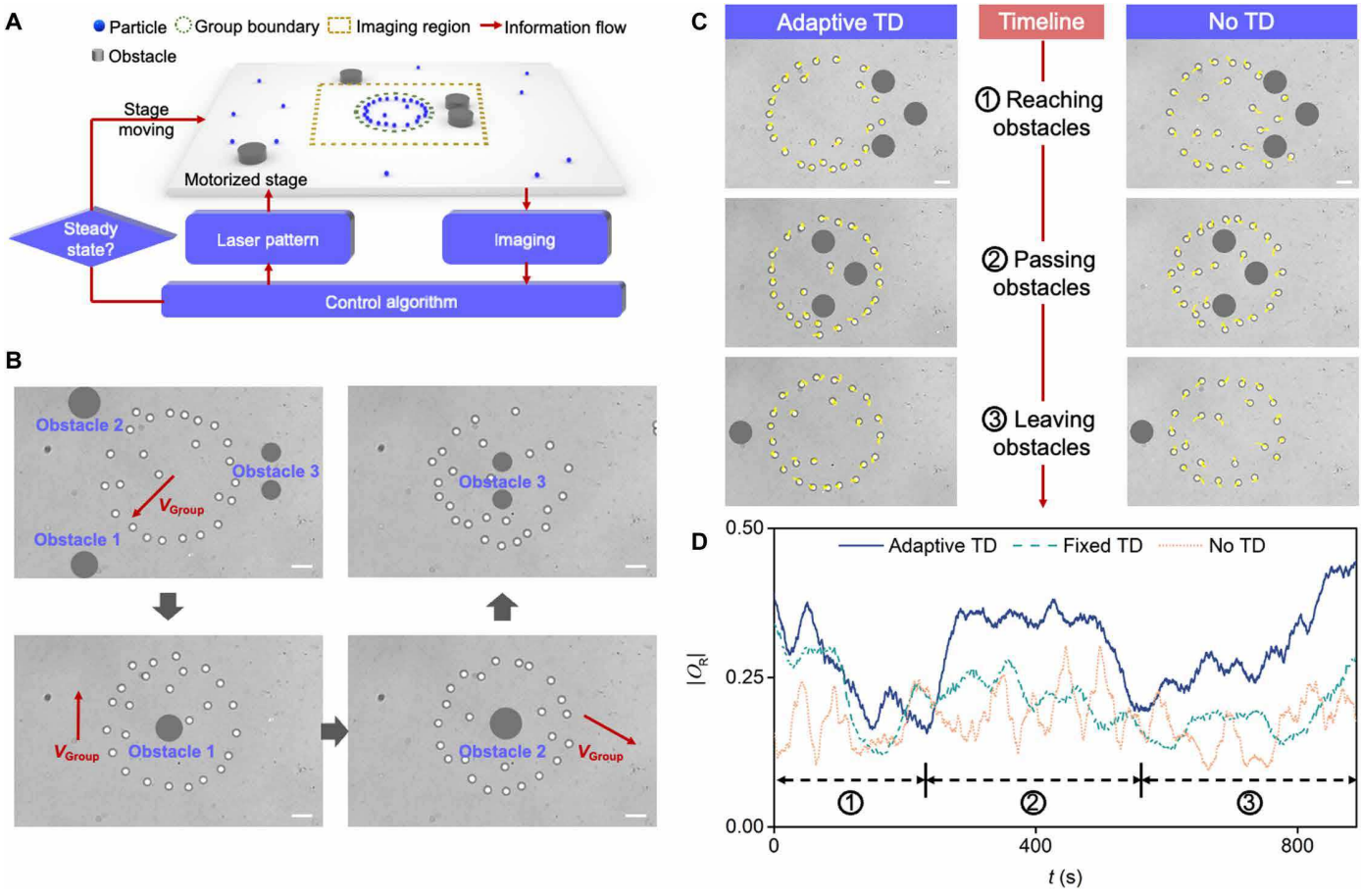

Fig. 5. Transportation of collective structures in complex environments under different time-delay conditions. (**A**) Schematic of the experimental setup for the long-distance delivery of collective structures. (**B**) Optical images showing the sequential passage of the collective structure through three sets of obstacles. The red arrow indicates the direction of movement for the entire group. Scale bar, 5 μm. (**C**) Two sets of optical images showing the collective structure navigates through the same obstacles with adaptive time delay (left) and without time delay (right), respectively. The parameters for the adaptive time delay are long $\tau = 1.0\tau^*$, short $\tau = 0.1\tau^*$, and $O_p^{local,*} = 0.4$. Scale bar, 5 μm. (**D**) The plot of $|O_R|$ versus time for the collective structure passing through the same obstacles shown in (C) under three different time-delay conditions. The parameters for the adaptive time-delay case are the same as those in (C), while the fixed time-delay case is based on the response time delay with $\tau = 1.0\tau^*$.

the achievement of responsive and persistent optical microrobots capable of operating in complex environments.

DISCUSSION

In this study, we introduce an adaptive time-delay strategy inspired by fish schools and use our optical feedback control experimental platform to investigate its impact on the persistence-responsivity tradeoff in collective motion. Initially, we develop an active perturbation method to quantitatively assess the persistence of collective structures. This method allows us to program particle's motion to replicate perturbations found in nature, such as searching for food sources or evading predators. Both experimental and simulated results demonstrate that a fixed time delay can enhance the persistence of collective motion in noisy environments, and a positive correlation between the time delay value and the persistence is confirmed. Next, we validate the persistence-responsivity tradeoff through experimental measurements. Furthermore, we apply an adaptive time delay with an improved threshold and observe an enhancement in the responsivity of collective structures by approximately 1.6 times in experiments while maintaining persistence. This enhancement, equivalent to results seen in prior studies (*36*), has the potential to reduce the time required for collective structures to reach a steady state by approximately 38%. Further improvements are possible through alternative mathematical models of the adaptive time delay strategy and the optimization of all relevant parameters (e.g., long and short τ) via more extensive parametric investigations. For the automated transportation of collective structures in complex environments, we integrate motorized stage control and obstacle-avoidance algorithms into the feedback control program. When navigating through the same obstacles, we observe more persistent and responsive collective motion under adaptive time delay, further confirming the effectiveness of the adaptive time-delay strategy.

It is important to note that the current collective structure, which orbits around a point, is not optimized for robotic applications. To achieve more efficient transportation of collective structures, future studies can imitate the leadership and hierarchy within living systems (*3*). Furthermore, while the effectiveness of the adaptive time-delay strategy has been established for rotational and translational collective motions, its performance in complex domains, characterized by

polygonal, elliptical, or irregular boundaries, remains uncertain. This uncertainty arises from the challenge of quantifying persistence and responsivity in such intricate spatial configurations. Addressing this aspect will be another key focus of future research endeavors. In conclusion, our proposed adaptive time delay offers an approach to addressing the inherent tradeoff between persistence and responsivity in collective motion. Moreover, the developed experimental platform enables fundamental investigations of collective motion in real-world settings and contributes to the advancement of swarm micro/nanorobotics.

MATERIALS AND METHODS

Sample preparation

The particle preparation follows the method outlined in (*48*). Briefly, unmodified silica microspheres with a mean diameter of 1.97 μm (Bangs Laboratories, SS04002) are used. The aqueous solution consists of 5 wt % polyethylene glycol (PEG; Sigma-Aldrich, 8.18897) and 5 wt % phosphate-buffered saline (PBS; Sigma-Aldrich, 806552). The substrate is a thermoplasmonic substrate coated with bovine serum albumin (BSA; Sigma-Aldrich, A8531). The process involves depositing a 5.5-nm gold film on a glass substrate using a thermal evaporator (Kurt J. Lesker, NANO 36) at a base pressure of 1×10^{-5} torr, with a deposition rate of 0.5 Å s^{-1}. The gold-coated substrate is then annealed at 550°C for 2 hours, resulting in the formation of randomly distributed gold nanoparticles. Subsequently, the thermoplasmonic substrate is immersed in 1 wt % BSA at room temperature for 1 day. Last, the solution is dropped onto the substrate and sealed with a spacer height of 0.12 mm.

Particles are propelled away from the laser spot along the substrate surface due to the interplay between thermoelectric and depletion forces. PBS provides essential ions, primarily Na^+ and Cl^-, for thermoelectric force generation (*48*). The differential drift rates of these ions ($v_{Na^+} > v_{Cl^-}$) result in an ionic redistribution around the laser-heated area, creating a thermoelectric field directed toward the hot spot. Consequently, the negatively charged SiO_2 particles are driven radially outward from this hot spot (fig. S12D). To retain the particles on the substrate for consistent imaging, PEG is introduced into the solution, inducing a depletion force that consistently drives particles toward the heat source. The concentration of PEG is precisely calibrated (*48*), ensuring that the depletion force is robust enough to work with the gravity to balance the thermoelectric force vertically while not forbidding the horizontal movement of particles. This force combination ensures that particles are always propelled away from the laser spot along the substrate surface.

Optical setup

The optical setup used in our experiment is illustrated in fig. S1. It involves a red laser (660 nm, Laser Quantum, Opus 660) that is expanded by a factor of 5 and directed toward a liquid crystal on silicon–spatial light modulator (SLM; Hamamatsu, X13138-01) with a resolution of 1392 × 1040 pixels. The SLM diffracts the laser based on holographic patterns generated by the computer. The diffracted laser pattern then passes through a 4f lens setup (with $f_1/f_2 = 0.75$) and reaches an inverted optical microscope (Nikon, Ti2). The microscope objective is an oil-based lens with ×60 magnification (Nikon, CFI Plan Fluor 60XS Oil). Optical images are captured using a charge-coupled device camera (Lumenera, INFINITY 2). In addition, a motorized stage (Prior, H117E1N5) is connected to the computer to enable automated long-distance transportation of the samples.

Feedback-control program

The control program used in our experiment is developed in LabVIEW (National Instruments, 2022 Q3) and serves as the central hub for controlling all computer-connected hardware. The program continuously captures real-time images from the optical setup and processes them. In the initial loop, all particles within the predefined circular confined geometry are identified and assigned a specific number for labeling (e.g., particle 1, particle 2, particle 3, etc.). From the second loop onward, as the particles typically move around 0.16 μm (corresponding to approximately 16% of the particle's radius) between two consecutive loops, all the particles can be steadily recognized and labeled with their initially assigned numbers by calculating the position difference between two neighboring image frames. This consistent labeling of particles is essential for calculating their real-time velocities and preserving their individual histories for time-delay interactions. The history of each particle is formed by sequentially storing its real-time velocity information.

After labeling the particles and obtaining their real-time velocities, the program determines the new direction for each particle using Eqs. 3 or 4 without factors $\mathscr{R}_\theta$ and $\mathscr{R}_\alpha$. However, in experimental settings, the time delay τ cannot be continuously controlled due to the nonnegligible time for imaging capture and data processing. Instead, we define τ as $\tau = n_\tau * \Delta t$, where $\Delta t \cong 0.132$ s and n_τ is a variable set in the program to control the value of τ. At the beginning of each experimental realization, we disable the time-delay Vicsek model for n_{loop} loops, during which the particles exhibit random motion. This allows sufficient time for each particle to accumulate enough history data for the calculation of Eqs. 3 or 4. In addition, the newly determined directions can be replaced by directions determined by volume exclusion or boundary reflection (discussed in subsequent sections) to avoid particle collisions or maintain the coherence of the collective structures.

On the basis of the newly determined directions of the particles, the spatial distribution of the laser pattern is determined. The laser beams are positioned permanently at the circumference of the particles, with a distance of 0.93 μm from the particle's center. The information regarding the positions of each laser is used to generate a hologram (*52*), which is then transmitted to the SLM and diffracts the input laser into laser patterns for controlling the collective motion of the particles.

To enable long-distance transportation, the movement of the motorized stage is also integrated into the control program. The communication between the stage and the computer is facilitated through the LabVIEW interface provided by the stage manufacturer. In the experimental setup, specific distances are programmed for the stage to move after a certain number of loops. For example, the stage can be instructed to move 0.15 μm in the X direction and 0.2 μm in the Y direction after eight loops (~1.06 s).

The LabVIEW control program also includes the calculation of the rotation order parameter, O_R. The program provides the option to export the calculated O_R values directly or output experimental videos and use a MATLAB-based video processing program to extract the corresponding values.

Time-delay Vicsek model

The time delay can be categorized into two types: the transmission time delay, resulting from the finite speed of information transmission among

agents, and the response time delay, arising from the finite speed of information processing and execution within each agent (*31*). Accordingly, the velocity $\mathbf{v}_i$ of particle i can be determined using either the transmission time delay (Eq. 3) or the response time delay (Eq. 4) (*12*)

$$\hat{\mathbf{v}}_i(t+\Delta t)=\mathscr{R}_\theta\mathscr{R}_\alpha\Theta\left[\hat{\mathbf{v}}_i(t)+\sum\nolimits_{j\in C_i(t-\tau)}\hat{\mathbf{v}}_j(t-\tau)\right] \quad (3)$$

$$\hat{\mathbf{v}}_i(t+\Delta t)=\mathscr{R}_\theta\mathscr{R}_\alpha\Theta\left[\hat{\mathbf{v}}_i(t-\tau)+\sum\nolimits_{j\in C_i(t-\tau)}\hat{\mathbf{v}}_j(t-\tau)\right] \quad (4)$$

where Δt represents the execution time of one feedback loop, $\mathscr{R}_\theta$ corresponds to a random rotation by an angle following a normal distribution, with the SD denoted as σ_θ (Fig. 2B and text S1). In our experimental conditions, the particle velocities not only fluctuate due to Brownian motion but also vary among particles due to size heterogeneity (fig. S2C). $\mathscr{R}_\alpha$ represents a rotation by an angle α due to long-range physical interactions exerted on the particle i by neighboring lasers (text S2). Note that the specific form of $\mathscr{R}_\alpha$ is based on the manipulation technique used for the particles (*48*). Different manipulation approaches (*49*, *53*) can modify or eliminate the factor $\mathscr{R}_\alpha$. The function $\Theta(\mathbf{v})\equiv\mathbf{v}/|\mathbf{v}|$ normalizes the vector $\mathbf{v}$. C_i represents the circular neighborhood around particle i with a radius of r_0, excluding particle i itself. τ denotes the time delay value. If we eliminate τ and $\mathscr{R}_\alpha$, then both equations reduce to the classic Vicsek model. Notably, in this experimental framework, Δt remains a fixed constant, primarily affecting the particle's movement in a probabilistic manner as outlined in text S1. Conversely, τ is adjustable, affecting the information transfer and subsequent pattern formation of the particles.

Volume exclusion

In the control program, the volume exclusion algorithm is incorporated to prevent particle collisions. This algorithm is triggered when a particle has at least one neighboring particle within a clearance distance of 1.91 μm. It is crucial to note that the clearance distance is measured from one particle's surface to the surface of the neighboring particle, i.e., the gap distance between the two particles. The new direction of the particle is then determined using Eq. 5 (*54*)

$$\hat{\mathbf{v}}_i(t+\Delta t)=-\mathscr{R}_\theta\mathscr{R}_\alpha\arg\left(\sum_{j\in C_i^{\mathrm{ve}}}^{i\neq j}\frac{\mathbf{r}_{ij}(t)}{|\mathbf{r}_{ij}(t)|}\right) \quad (5)$$

Here, C_i^{ve} represents the repelling zone of particle i, and $\mathbf{r}_{ij}(t)$ is the vector pointing from particle i to its neighbor j. Referring to the concept of adaptive time delay, the particle having potentially colliding particle(s) around is similar to a disordered neighboring environment, both of which will make the particle alert and respond fast. As also mentioned in (*54*), the volume exclusion has a higher priority than the velocity alignment. Consequently, we assume that particles can instantly achieve volume exclusion. This implies that, aside from the inherent instrumental delay introduced by image capture and data processing, the control algorithm refrains from adding any extra time delay in "volume exclusion" to prevent potential collisions.

Boundary condition

The control program also incorporates a reflective boundary condition to ensure the coherence of the collective structure. When a particle's distance to the center of the geometry ($|\mathbf{r}_{i-\mathrm{b}}(t)|$) exceeds the radius of the circular geometry (r_b), the particle is considered to interact with the boundary. However, since there is an execution time for each loop, $|\mathbf{r}_{i-\mathrm{b}}(t)|$ can exceed r_b between two loops. To account for this, an interaction thickness (Δr_b) is introduced. Whenever $|\mathbf{r}_{i-\mathrm{b}}(t)|$ falls within the range $[r_\mathrm{b}, r_\mathrm{b}+\Delta r_\mathrm{b}]$, the boundary reflection takes effect for particle i. The new direction of the particle is determined using Eq. 6 (*11*)

$$\hat{v}_i(t+\Delta t)=\mathscr{R}_\theta\mathscr{R}_\alpha\Theta\left[\hat{v}_i(t)-2\left(\hat{v}_i(t)\bullet\frac{\mathbf{r}_{i-\mathrm{b}}(t)}{|\mathbf{r}_{i-\mathrm{b}}(t)|}\right)\frac{\mathbf{r}_{i-\mathrm{b}}(t)}{|\mathbf{r}_{i-\mathrm{b}}(t)|}\right] \quad (6)$$

r_b and Δr_b are set to be 20.0 and 0.39 μm, respectively. However, because of the long-range laser-induced repelling forces in our current particle manipulation technique (see text S2), the particle can be occasionally pushed out of the boundary, i.e., $|\mathbf{r}_{i-\mathrm{b}}(t)|>(r_\mathrm{b}+\Delta r_\mathrm{b})$. When this situation occurs, the new direction is set to $\hat{\mathbf{v}}_i(t+\Delta t)=-\mathscr{R}_\theta\mathscr{R}_\alpha\frac{\mathbf{r}_{i-\mathrm{b}}(t)}{|\mathbf{r}_{i-\mathrm{b}}(t)|}$. Like the volume exclusion algorithm, besides inherent instrumental time delay, the control program does not introduce any extra time delay in the "boundary reflection" to prevent particles from escaping the boundary.

Supplementary information of adaptive time-delay strategy

As shown in Eq. 1, we assume that the current time delay is decided by $O_\mathrm{P}^{\mathrm{local}}$ of the previous execution loop. This is because, intuitively, the agents can decide to become calm or alerted in the future only after assessing the current surrounding environment. Once the time delay τ is resolved, the agents retrieve information from their memories and execute the time-delay Vicsek model as per Eq. 4. Simultaneously, the agents use the same information to assess their surrounding environment and determine the value of $O_\mathrm{P}^{\mathrm{local}}$ at time t

$$O_\mathrm{P}^{\mathrm{local}}(t)=\begin{cases}\frac{1}{N_{\mathrm{local}}}\left|\hat{\mathbf{v}}_i(t-\mathrm{short}\,\tau)+\sum_{j\in C_i}\hat{\mathbf{v}}_j(t-\mathrm{short}\,\tau)\right|, & O_\mathrm{P}^{\mathrm{local}}(t-\Delta t)<O_\mathrm{P}^{\mathrm{local},*}\\ \frac{1}{N_{\mathrm{local}}}\left|\hat{\mathbf{v}}_i(t-\mathrm{long}\,\tau)+\sum_{j\in C_i}\hat{\mathbf{v}}_j(t-\mathrm{long}\,\tau)\right|, & O_\mathrm{P}^{\mathrm{local}}(t-\Delta t)\geq O_\mathrm{P}^{\mathrm{local},*}\end{cases} \quad (7)$$

In both experiments and simulations, the initial condition is determined by the following rule: When $0\leq t\leq \mathrm{long}\,\tau$, all particles engage in random movements instead of executing the Vicsek model. This allows them to accumulate their initial "memories" of the system. At $t=\mathrm{long}\,\tau+\Delta t$, it is assumed that every particle has a time delay of long τ. From this point onward, the particles autonomously adhere to the adaptive time-delay strategy based on Eqs. 1 and 7 for their future movements.

Modeling and simulations of collective motion

In the computational modeling, there are seven key components: the time-delay Vicsek model, volume exclusion, boundary reflection, long-range physical interaction, Brownian motion, particle heterogeneity, and laser-positioning deviation. In each simulation loop, the ideal moving direction of each particle is determined by the time-delay Vicsek model (Eqs. 3 and 4 without considering $\mathscr{R}_\theta$ and $\mathscr{R}_\alpha$). In addition, the potential volume exclusion effect is considered (Eq. 5 without considering $\mathscr{R}_\theta$ and $\mathscr{R}_\alpha$), as well as the potential boundary reflection (Eq. 6 without considering $\mathscr{R}_\theta$ and $\mathscr{R}_\alpha$). These factors collectively determine the ideal movement direction of each particle at the beginning of the simulation loop. Once the ideal movement direction is determined, the laser position for each

particle is accurately resolved, resulting in the determination of $\theta_{i,\mathrm{laser}}(t)$ for each particle.

In the context of collective motion in the real world, the movement of each particle is also influenced by three factors: Brownian motion (text S1), particle heterogeneity (fig. S2), and long-range physical interaction (text S2). These factors can be incorporated into the computational modeling using the following Langevin equations

$$|\mathbf{v}_{i,\parallel}(t)| = |\mathbf{v}_{i,\mathrm{laser\_tot}}(t)|\cos\delta + \sqrt{2D_i}\xi_{\parallel}(t) \tag{8}$$

$$|\mathbf{v}_{i,\parallel}(t)| = |\mathbf{v}_{i,\mathrm{laser\_tot}}(t)|\cos\delta + \sqrt{2D_i}\xi_{\parallel}(t) \tag{9}$$

Here, $\mathbf{v}_i(t)$ is decomposed based on the direction of $\theta_{i,\mathrm{laser\_tot}}(t)$ to obtain $\mathbf{v}_{i,\parallel}(t)$ and $\mathbf{v}_{i,\perp}(t)$, where $\mathbf{v}_{i,\parallel}(t)$ is parallel to the direction of $\theta_{i,\mathrm{laser\_tot}}(t)$. The parameter δ is used in Eqs. 8 and 9 to account for the influence of Brownian motion and is independent of $\theta_{i,\mathrm{laser\_tot}}(t)$. D_i represents the diffusion coefficient of particle i, which varies among different particles due to particle heterogeneity (fig. S2B). The characterization of δ and D can be found in text S1. In addition, the total velocity induced by the laser, including the laser following particle i and the neighboring lasers due to the long-range physical interactions, can be expressed as

$$\mathbf{v}_{i,\mathrm{laser\_tot}}(t) = \mathbf{v}_{i,\mathrm{laser}} + \sum \mathbf{v}_{j-i,\mathrm{laser}}(t) \tag{10}$$

$\mathbf{v}_{i,\mathrm{laser}}$ is the velocity induced by the laser placed at the circumference of the particle i, which varies among particles due to the particle heterogeneity (fig. S2C). $\mathbf{v}_{j-i,\mathrm{laser}}(t)$ is the additional velocity induced by the neighboring lasers. The magnitude and direction of $\mathbf{v}_{j-i,\mathrm{laser}}(t)$ can be determined by the following equations

$$|\mathbf{v}_{j-i,\mathrm{laser}}(t)| = \frac{Cd_{j-i}(t)}{[d_{j-i}(t)]^2 + R^2}\frac{|\mathbf{v}_{i,\mathrm{laser}}|}{|\mathbf{v}_{\mathrm{avg,laser}}|} \tag{11}$$

$$\theta_{j-i,\mathrm{laser}}(t) = \theta_{i,\mathrm{laser}}(t) + \mathrm{asin}\left\{\frac{R}{d_{j-i}(t)}\sin[\theta_{i,\mathrm{laser}}(t) - \theta_{j,\mathrm{laser}}(t)]\right\} \tag{12}$$

The Eq. 11 is modified based on eq. S5 in text S2, where the fitting parameter $C = 1.74$ μm/s, the radius of the particle $R = 0.985$ μm, and the average velocity of the particle $|\mathbf{v}_{\mathrm{avg,laser}}| = 1.16$ μm/s when the laser-particle distance $d = 0.93$ μm. $\frac{|\mathbf{v}_{i,\mathrm{laser}}|}{|\mathbf{v}_{\mathrm{avg,laser}}|}$ serves as a normalization factor that adjusts the laser influence on the particle i based on particle heterogeneity. The distance between the center of the particle i and the neighboring laser that follows particle j [i.e., $d_{j-i}(t)$] can be expressed as

$$d_{j-i}(t) = \sqrt{R^2 + [d_{j-i,\mathrm{center}}(t)]^2 - 2Rd_{j-i,\mathrm{center}}(t)\cos[\theta_{i,\mathrm{laser}}(t) - \theta_{j,\mathrm{laser}}(t)]} \tag{13}$$

Here, $d_{j-i,\mathrm{center}}(t)$ is the distance between the geometric center of particle i and the geometric center of particle j, which can be easily determined in simulations.

Moreover, the laser-positioning deviation can also be integrated into the simulations by modifying Eqs. 12 and 13

$$X_{j-i,\mathrm{laser}}(t) = d_{j-i}(t) \bullet \cos\theta_{j-i,\mathrm{laser}}(t) + \Delta x \tag{14}$$

$$Y_{j-i,\mathrm{laser}}(t) = d_{j-i}(t) \bullet \sin\theta_{j-i,\mathrm{laser}}(t) + \Delta y \tag{15}$$

$$d'_{j-i}(t) = \sqrt{X_{j-i,\mathrm{laser}}(t)^2 + Y_{j-i,\mathrm{laser}}(t)^2} \tag{16}$$

$$\theta'_{j-i,\mathrm{laser}}(t) = \mathrm{atan2}[Y_{j-i,\mathrm{laser}}(t), X_{j-i,\mathrm{laser}}(t)] \tag{17}$$

Δx and Δy is the laser-positioning deviation in the x and y directions defined in the imaging plane.

In simulation condition 2, $\Delta x = \Delta y = 0.0775$ μm is set, which is equal to the one-pixel deviation in two directions, respectively. In simulation condition 3, σ_δ is increased from 0.24 to 0.36 μm/s, determined by the fitting in fig. S4A. A larger σ_δ leads to a more disordered collective pattern, which deviates from experimental observations.

For each simulation data point, averaging is performed over at least 20 realizations with different initial states. A single realization consists of 12,000 timesteps, and the last 6000 data points are averaged to obtain $\langle|O_R|\rangle$, ensuring that $\langle|O_R|\rangle$ is obtained at the steady state. The active perturbation is activated at the 8000th timestep, occurring after the collective structure reaches its steady state. For experiments, each data point shown with SD is averaged over at least eight realizations.

To model the two-dimensional translational collective motion in open space, we remain the components of the time-delay Vicsek model, volume exclusion, Brownian motion, and particle heterogeneity, as previously outlined in Eqs. 1 to 9. In addition, we incorporate an attraction force within Eq. 4 to ensure the collective structure's cohesion, detailed in (*54*, *55*)

$$\hat{v}_i(t+\Delta t) = \mathscr{R}_\theta\mathscr{R}_\alpha\Theta\begin{bmatrix}\hat{\mathbf{v}}_i(t-\tau) + \sum_{j\in C_i(t-\tau)}\hat{\mathbf{v}}_j(t-\tau) \\ +\gamma\sum_{j\in C_i^{\mathrm{attract}}(t-\tau)}\mathbf{n}_{ji}(t-\tau)\end{bmatrix} \tag{18}$$

Here, γ denotes the strength of attraction, which is set at 0.1 for our simulations. The attraction zone for particle i, $C_i^{\mathrm{attract}}(t-\tau)$, is conceptualized as a ring domain where $r_{ij} \in [r_0, 2r_0]$. The unit vector from particle i to particle j at time $t-\tau$, $\mathbf{n}_{ij}(t-\tau)$, is given by $\frac{\mathbf{r}_{ij}(t-\tau)}{|\mathbf{r}_{ij}(t-\tau)|}$. According to (*36*), we quantify the persistence of the collective structure in open space by the average angular deviation ($\langle\langle(\Delta\phi)^2\rangle\rangle$) from its initial to subsequent movement directions, gauging its directional stability against trivial perturbations (e.g., Brownian motion). In each simulation, $\Delta\phi$ is calculated by comparing the collective's average movement direction during the time intervals 7950 to 8000 with that from 950 to 1000. We determine the group velocity, V_g, by dividing the net distance traveled from timestep 1 to 8000 by the elapsed time. Consequently, in Fig. 4E, data points for $O_P^{\mathrm{local},*} > 0.8$ are absent due to the collective structure's diminished directionality above this threshold, where the net distance may approach zero under certain extreme

conditions. For each simulation data point in Fig. 4 (D to F), averaging is performed over at 200 realizations with different initial states.

Supplementary Materials

This PDF file includes:

Supplementary Text S1 to S5
Figs. S1 to S14
Tables S1 and S2
Legends for movies S1 to S9
References

Other Supplementary Material for this manuscript includes the following:

Movies S1 to S9

REFERENCES AND NOTES

1. T. Vicsek, A. Zafeiris, Collective motion. *Phys. Rep.* **517**, 71–140 (2012).
2. F. Ji, Y. Wu, M. Pumera, L. Zhang, Collective behaviors of active matter learning from natural taxes across scales. *Adv. Mater.* **35**, 2203959 (2022).
3. M. Nagy, Z. Ákos, D. Biro, T. Vicsek, Hierarchical group dynamics in pigeon flocks. *Nature* **464**, 890–893 (2010).
4. J. Jhawar, R. G. Morris, U. R. Amith-Kumar, M. Danny Raj, T. Rogers, H. Rajendran, V. Guttal, Noise-induced schooling of fish. *Nat. Phys.* **16**, 488–493 (2020).
5. J. Buhl, D. J. T. Sumpter, I. D. Couzin, J. J. Hale, E. Despland, E. R. Miller, S. J. Simpson, From disorder to order in marching locusts. *Science* **312**, 1402–1406 (2006).
6. K. Zhang, P. Chermprayong, F. Xiao, D. Tzoumanikas, B. Dams, S. Kay, B. B. Kocer, A. Burns, L. Orr, C. Choi, D. D. Darekar, W. Li, S. Hirschmann, V. Soana, S. A. Ngah, S. Sareh, A. Choubey, L. Margheri, V. M. Pawar, R. J. Ball, C. Williams, P. Shepherd, S. Leutenegger, R. Stuart-Smith, M. Kovac, Aerial additive manufacturing with multiple autonomous robots. *Nature* **609**, 709–717 (2022).
7. G. Vásárhelyi, C. Virágh, G. Somorjai, T. Nepusz, A. E. Eiben, T. Vicsek, Optimized flocking of autonomous drones in confined environments. *Sci. Robot.* **3**, eaat3536 (2018).
8. T. Vicsek, A. Czirók, E. Ben-Jacob, I. Cohen, O. Shochet, Novel type of phase transition in a system of self-driven particles. *Phys. Rev. Lett.* **75**, 1226–1229 (1995).
9. C. A. Yates, R. Erban, C. Escudero, I. D. Couzin, J. Buhl, I. G. Kevrekidis, P. K. Maini, D. J. T. Sumpter, Inherent noise can facilitate coherence in collective swarm motion. *Proc. Natl. Acad. Sci. U.S.A.* **106**, 5464–5469 (2009).
10. M. L. Rubio Puzzo, A. De Virgiliis, T. S. Grigera, Self-propelled Vicsek particles at low speed and low density. *Phys. Rev. E* **99**, 052602 (2019).
11. D. Armbruster, S. Motsch, A. Thatcher, Swarming in bounded domains. *Phys. D: Nonlinear Phenom.* **344**, 58–67 (2017).
12. V. Holubec, D. Geiss, S. A. M. Loos, K. Kroy, F. Cichos, Finite-size scaling at the edge of disorder in a time-delay Vicsek model. *Phys. Rev. Lett.* **127**, 258001 (2021).
13. H. Murakami, C. Feliciani, Y. Nishiyama, K. Nishinari, Mutual anticipation can contribute to self-organization in human crowds. *Sci. Adv.* **7**, eabe7758 (2021).
14. M. Durve, A. Saha, A. Sayeed, Active particle condensation by non-reciprocal and time-delayed interactions. *Eur. Phys. J. E* **41**, 49 (2018).
15. H. Murakami, T. Niizato, Y.-P. Gunji, Emergence of a coherent and cohesive swarm based on mutual anticipation. *Sci. Rep.* **7**, 46447 (2017).
16. P. Gerlee, K. Tunstrøm, T. Lundh, B. Wennberg, Impact of anticipation in dynamical systems. *Phys. Rev. E* **96**, 062413 (2017).
17. P. Yang, M. Liu, X. Lei, C. Song, A novel control algorithm for the self-organized fission behavior of flocking system with time delay. *Int. J. Control, Autom. and Syst.* **14**, 986–997 (2016).
18. R. Erban, J. Haškovec, Y. Sun, A Cucker--Smale Model with Noise and Delay. *SIAM J. Appl. Math.* **76**, 1535–1557 (2016).
19. A. Morin, J.-B. Caussin, C. Eloy, D. Bartolo, Collective motion with anticipation: Flocking, spinning, and swarming. *Phys. Rev. E* **91**, 012134 (2015).
20. L. C. Davis, Modifications of the optimal velocity traffic model to include delay due to driver reaction time. *Phys. A: Stat. Mech. Appl.* **319**, 557–567 (2003).
21. H. L. More, J. M. Donelan, Scaling of sensorimotor delays in terrestrial mammals. *Proc. R. Soc. B: Biol. Sci.* **285**, 20180613 (2018).
22. M. Leyman, F. Ogemark, J. Wehr, G. Volpe, Tuning phototactic robots with sensorial delays. *Phys. Rev. E* **98**, 052606 (2018).
23. K. Szwaykowska, I. B. Schwartz, L. Mier-y-Teran Romero, C. R. Heckman, D. Mox, M. A. Hsieh, Collective motion patterns of swarms with delay coupling: Theory and experiment. *Phys. Rev. E* **93**, 032307 (2016).
24. C. Virágh, G. Vásárhelyi, N. Tarcai, T. Szörényi, G. Somorjai, T. Nepusz, T. Vicsek, Flocking algorithm for autonomous flying robots. *Bioinspir. Biomim.* **9**, 025012 (2014).
25. B. Rahman, K. B. Blyuss, Y. N. Kyrychko, Dynamics of neural systems with discrete and distributed time delays. *SIAM J. Appl. Dyn. Syst.* **14**, 2069–2095 (2015).
26. L. Giuggioli, T. J. McKetterick, M. Holderied, Delayed response and biosonar perception explain movement coordination in trawling bats. *PLOS Comput. Biol.* **11**, e1004089 (2015).
27. B. G. Borghuis, A. Leonardo, The role of motion extrapolation in amphibian prey capture. *J. Neurosci.* **35**, 15430–15441 (2015).
28. G. Vásárhelyi, C. Virágh, G. Somorjai, N. Tarcai, T. Szörenyi, T. Nepusz, T. Vicsek, Outdoor flocking and formation flight with autonomous aerial robots. *IEEE/RSJ Int. Conf. Intell. Robots Syst.* **3866-3873**, (2014).
29. E. Forgoston, I. B. Schwartz, Delay-induced instabilities in self-propelling swarms. *Phys. Rev. E* **77**, 035203 (2008).
30. R. Piwowarczyk, M. Selin, T. Ihle, G. Volpe, Influence of sensorial delay on clustering and swarming. *Phys. Rev. E* **100**, 012607 (2019).
31. Y. Sun, W. Li, L. Li, G. Wen, S. Azaele, W. Lin, Delay-induced directional switches and mean switching time in swarming systems. *Phys. Rev. Res.* **4**, 033054 (2022).
32. J. Hindes, K. Szwaykowska, I. B. Schwartz, Hybrid dynamics in delay-coupled swarms with mothership networks. *Phys. Rev. E* **94**, 032306 (2016).
33. M. Mijalkov, A. McDaniel, J. Wehr, G. Volpe, Engineering sensorial delay to control phototaxis and emergent collective behaviors. *Phys. Rev. X* **6**, 011008 (2016).
34. Y. Sun, W. Lin, R. Erban, Time delay can facilitate coherence in self-driven interacting-particle systems. *Phys. Rev. E* **90**, 062708 (2014).
35. D. Geiß, K. Kroy, V. Holubec, Signal propagation and linear response in the delay Vicsek model. *Phys. Rev. E* **106**, 054612 (2022).
36. B. Balázs, G. Vásárhelyi, T. Vicsek, Adaptive leadership overcomes persistence–responsivity trade-off in flocking. *J. R. Soc. Interface* **17**, 20190853 (2020).
37. J. Sawicki, R. Berner, S. A. Loos, M. Anvari, R. Bader, W. Barfuss, N. Botta, N. Brede, I. Franović, D. J. Gauthier, Perspectives on adaptive dynamical systems. arXiv preprint arXiv:2303.01459, (2023).
38. B. C. Daniels, D. C. Krakauer, J. C. Flack, Control of finite critical behaviour in a small-scale social system. *Nat. Commun.* **8**, 14301 (2017).
39. W. Poel, B. C. Daniels, M. M. G. Sosna, C. R. Twomey, S. P. Leblanc, I. D. Couzin, P. Romanczuk, Subcritical escape waves in schooling fish. *Sci. Adv.* **8**, eabm6385 (2022).
40. H. Zhao, H. Liu, Y. W. Leung, X. Chu, Self-adaptive collective motion of swarm robots. *IEEE Trans Autom Sci Eng* **15**, 1533–1545 (2018).
41. U. Khadka, V. Holubec, H. Yang, F. Cichos, Active particles bound by information flows. *Nat. Commun.* **9**, 3864 (2018).
42. F. A. Lavergne, H. Wendehenne, T. Bäuerle, C. Bechinger, Group formation and cohesion of active particles with visual perception–dependent motility. *Science* **364**, 70–74 (2019).
43. T. Bäuerle, R. C. Löffler, C. Bechinger, Formation of stable and responsive collective states in suspensions of active colloids. *Nat. Commun.* **11**, 2547 (2020).
44. X. Wang, P.-C. Chen, K. Kroy, V. Holubec, F. Cichos, Spontaneous vortex formation by microswimmers with retarded attractions. *Nat. Commun.* **14**, 56 (2023).
45. T. Bäuerle, A. Fischer, T. Speck, C. Bechinger, Self-organization of active particles by quorum sensing rules. *Nat. Commun.* **9**, 3232 (2018).
46. R. C. Löffler, T. Bäuerle, M. Kardar, C. M. Rohwer, C. Bechinger, Behavior-dependent critical dynamics in collective states of active particles. *EPL* **134**, 64001 (2021).
47. C.-J. Chen, C. Bechinger, Collective response of microrobotic swarms to external threats. *New J. Phys.* **24**, 033001 (2022).
48. H. Ding, Z. Chen, P. S. Kollipara, Y. Liu, Y. Kim, S. Huang, Y. Zheng, Programmable multimodal optothermal manipulation of synthetic particles and biological cells. *ACS Nano* **16**, 10878–10889 (2022).
49. M. Fränzl, S. Muiños-Landin, V. Holubec, F. Cichos, Fully Steerable symmetric thermoplasmonic microswimmers. *ACS Nano* **15**, 3434–3440 (2021).
50. K. Tunstrøm, Y. Katz, C. C. Ioannou, C. Huepe, M. J. Lutz, I. D. Couzin, Collective states, multistability and transitional behavior in schooling fish. *PLOS Comput. Biol.* **9**, e1002915 (2013).
51. D. Geiss, K. Kroy, V. Holubec, Brownian molecules formed by delayed harmonic interactions. *New J. Phys.* **21**, 093014 (2019).
52. R. W. Bowman, G. M. Gibson, A. Linnenberger, D. B. Phillips, J. A. Grieve, D. M. Carberry, S. Serati, M. J. Miles, M. J. Padgett, "Red Tweezers": Fast, customisable hologram generation for optical tweezers. *Comput. Phys. Commun.* **185**, 268–273 (2014).
53. H. Ding, P. S. Kollipara, K. Yao, Y. Chang, D. J. Dickinson, Y. Zheng, Multimodal Optothermal Manipulations along Various Surfaces. *ACS Nano* **17**, 9280–9289 (2023).
54. I. D. Couzin, J. Krause, R. James, G. D. Ruxton, N. R. Franks, Collective memory and spatial sorting in animal groups. *J. Theor. Biol.* **218**, 1–11 (2002).
55. F. Ginelli, The Physics of the Vicsek model. *Eur. Phys. J. Spec. Top.* **225**, 2099–2117 (2016).
56. A. Zöttl, H. Stark, Hydrodynamics determines collective motion and phase behavior of active colloids in quasi-two-dimensional confinement. *Phys. Rev. Lett.* **112**, 118101 (2014).

57. M. C. Marchetti, J. F. Joanny, S. Ramaswamy, T. B. Liverpool, J. Prost, M. Rao, R. A. Simha, Hydrodynamics of soft active matter. *Rev. Mod. Phys.* **85**, 1143–1189 (2013).

Acknowledgments: We thank K. Yao and Y. Kim for stimulating discussions. **Funding:** This work was supported by National Science Foundation NSF-ECCS-2001650 and the National Institute of General Medical Sciences of the National Institutes of Health R01GM146962.
Author contributions: Conceptualization: Z.C. and Y.Z. Methodology: Z.C. and Y.Z. Investigation: Z.C. and Y.Z. Visualization: Z.C. Supervision: Y.Z. Writing—original draft: Z.C. Writing—review and editing: Z.C. and Y.Z. **Competing interests:** The authors declare that they have no competing interests. **Data and materials availability:** All data needed to evaluate the conclusions in the paper are present in the paper and/or the Supplementary Materials.

Submitted 18 August 2023
Accepted 29 February 2024
Published 3 April 2024
10.1126/sciadv.adk3914